J Mater Sci (2017) 52:519–532

Ceria-based electrolytes with high surface area and improved conductivity for intermediate temperature solid oxide fuel cells

P. Ramos-Alvarez[1,*], M. E. Villafuerte-Castrejón[1], G. González[1], M. Cassir[2], C. Flores-Morales[1], and J. A. Chávez-Carvayar[1]

[1] *Instituto de Investigaciones en Materiales, UNAM, Circuito Exterior s/n. Ciudad Universitaria, C. P. 04510 México, DF, Mexico*
[2] *Institut de Recherche de Chimie Paris, IRCP, UMR 8247 du CNRS, Chimie ParisTech (PSL), ENSCP, 11 rue Pierre et Marie Curie, 75231 Paris Cedex 05, France*

Received: 27 May 2016
Accepted: 26 August 2016
Published online: 9 September 2016

ABSTRACT

High-purity-doped ceria compounds $Ce_{1-x}RE_xO_{2-\delta}$ (RE = Sm, Gd; $0 \leq x \leq 0.30$) were synthesized by the Pechini method at 400 °C. Nanostructured products of crystallite size 5–11 nm were obtained, presenting a single fluorite cubic phase and high surface area values in the range of 75–110 m^2g^{-1}. Dense ceramic products with a relative density of 96–98 % resulted after sintering at 1450 °C. Impedance spectroscopy was used to study the conductivity of these compounds in the temperature range of 200–750 °C. Between 600 and 730 °C, the compounds with $x = 0.15$, 0.20 show conductivities on the order of 10^{-1} Scm^{-1}, with activation energies between 0.9 and 1.1 eV. Surface areas and conductivity values were found to be comparable with the highest values reported in the literature for similar compounds.

Introduction

The search of a way to generate electric energy in a clean and efficient manner is a critical economical and technological challenge, which arises from the need to conserve natural resources while reducing ecological impact from energy production [1–3]. Fuel cells are a promising avenue of research into finding the solution to this problem, in particular solid oxide fuel cells (SOFC), which are conformed by three main elements: an anode, an electrolyte, and a cathode; all three elements are made from ceramic materials.

SOFCs are an excellent alternative for energy production from "non-renewable" traditional means (based on the combustion of fossil fuels), because they do not emit pollutants (NO_x, SO_x, CO_2), have low sound pollution level (without noise, vibrations), and they possess a strong advantage over "renewable" means such as hydroelectric or wind and solar, since fuel cells can be operated on-demand regardless of time of the year. They are also capable of reaching high operating efficiencies since they convert chemical energy directly into electricity via an electrochemical process without any intermediate steps [4].

Address correspondence to E-mail: paolaeramosalvarez@gmail.com

DOI 10.1007/s10853-016-0350-5

For the construction of the cell, the solid electrolyte should satisfy important requirements, i.e., good ionic transport, thermodynamic stability over a wide range of temperatures in oxygen partial pressure, thermal expansion coefficient compatible with both electrodes, among other properties. A present challenge in the implementation of these devices is the development of materials which can operate effectively at a temperature range of 500–800 °C (the current operating temperature is over 1000 °C), maintaining adequate conductivity for its functioning, on the order of $\sigma_{ion} \sim 10^{-1}$ Scm^{-1}, and still keeping a high enough temperature for internal fuel reforming. Reducing the operating temperature brings the all-around benefits of prolonging the useful life of the cells, lowering costs. Electricity generated becomes cheaper and investment in the materials used in cell construction is shifted toward more common alloys than used at present [5]. These cells are known as intermediate temperature solid oxide fuel cells (IT–SOFCs) [6].

The most common material used as solid electrolyte in commercial SOFCs is yttria-stabilized zirconia (YSZ), with an operating temperature of 1000 °C [7, 8]; however, diverse electrolytes have been used in this type of cells as an alternative to this compound, these can be seen in the following table:

Type	Composition	Conductivity (Scm^{-1})	Temperature (°C)	Reference
Zirconia-based electrolytes	6–11 mol.% Sc_2O_3–ZrO_2	$1.8–3.4 \times 10^{-1}$	1000	[9–11]
	$Zr_{0.84}Ca_{0.16}O_{1.85}$	$\sim 10^{-2}$	1000	[12]
Lanthanum-based electrolytes	$La_{0.9}Sr_{0.1}Ga_{0.76}Mg_{0.19}Co_{0.05}O_3$	4×10^{-1}	1000	[13]
	$La_{0.9}Sr_{0.1}Ga_{0.76}Mg_{0.19}Fe_{0.05}O_3$	4.4×10^{-1}	1000	[13]
	$La_{0.9}Sr_{0.1}Al_{0.9}Mg_{0.1}O_{3-\delta}$	7×10^{-1}	1000	[14, 15]
Ceria-based electrolytes	$Ce_{1-x}Gd_xO_{2-\delta}$ ($x = 0.10–0.25$)	5×10^{-3}–4.1×10^{-2}	600–700	[16–18]
	$Ce_{1-x}Sm_xO_{2-\delta}$ ($x = 0.10–0.20$)	5.7×10^{-3}–8.8×10^{-2}	600–800	[19, 20]
	$Ce_{0.8}Y_{0.2}O_{1.9}$	3.4×10^{-2}	700	[21]
	Ca, Nd doped CeO_2	10^{-2}	600	[22]

Rare-earth doped CeO_2 exhibits superior ionic conductivity (O^{2-}) at temperatures of 600–1000 °C, and lower activation energy [23–25] in comparison with YSZ; however, it is still necessary to improve the conductivity in the intermediate temperature range mentioned before. This improvement is achieved with modifications to the structure, physical and chemical properties through a careful synthesis method [26]. Doped ceria compounds can be produced by synthesis methods such as combustion [27], surfactant-assisted [28], hydrothermal [29, 30], hydrothermal microwave-assisted [31], chemical precipitation [32], coprecipitation [33], freeze-dried precursors [34], sol–gel [35], and citrate methods [36]; the latter two methods have provided the highest purity and homogeneity. In this work, nanometric powders of solid solutions of $Ce_{1-x}Gd_xO_{2-\delta}$ (GDC) and $Ce_{1-x}Sm_xO_{2-\delta}$ (SDC) with $0 \leq x \leq 0.30$ were obtained via the Pechini method, in a fast and low cost way, improving homogeneity of the compounds, reducing particle size and porosity, increasing surface areas, and with a conductivity of 10^{-1} Scm^{-1} between 600 and 730 °C.

Materials and methods

Sample preparation

$Ce(NO_3)_3{\cdot}6H_2O$ (Sigma-Aldrich 99.99 %), $Sm(NO_3)_3{\cdot}6H_2O$ (Sigma-Aldrich 99.9 %), $Gd(NO_3)_3{\cdot}6H_2O$ (Sigma-Aldrich 99.9 %), citric acid (Sigma-Aldrich 99 %), and ethylene glycol anhydrous (Sigma-Aldrich 99.8 %) were used as starting reagents. The required amount of each salt for obtaining the desired quantity of product was stoichiometrically calculated with basis on the formula:

$$(1-x)\ Ce(NO_3)_3 \cdot 6H_2O + (x)RE(NO_3)_3 \cdot 6H_2O \rightarrow Ce_{1-x}RE_xO_{2-\delta}. \quad (1)$$

The metallic salts were dissolved in distilled water at 0.5 molar, under constant stirring at room

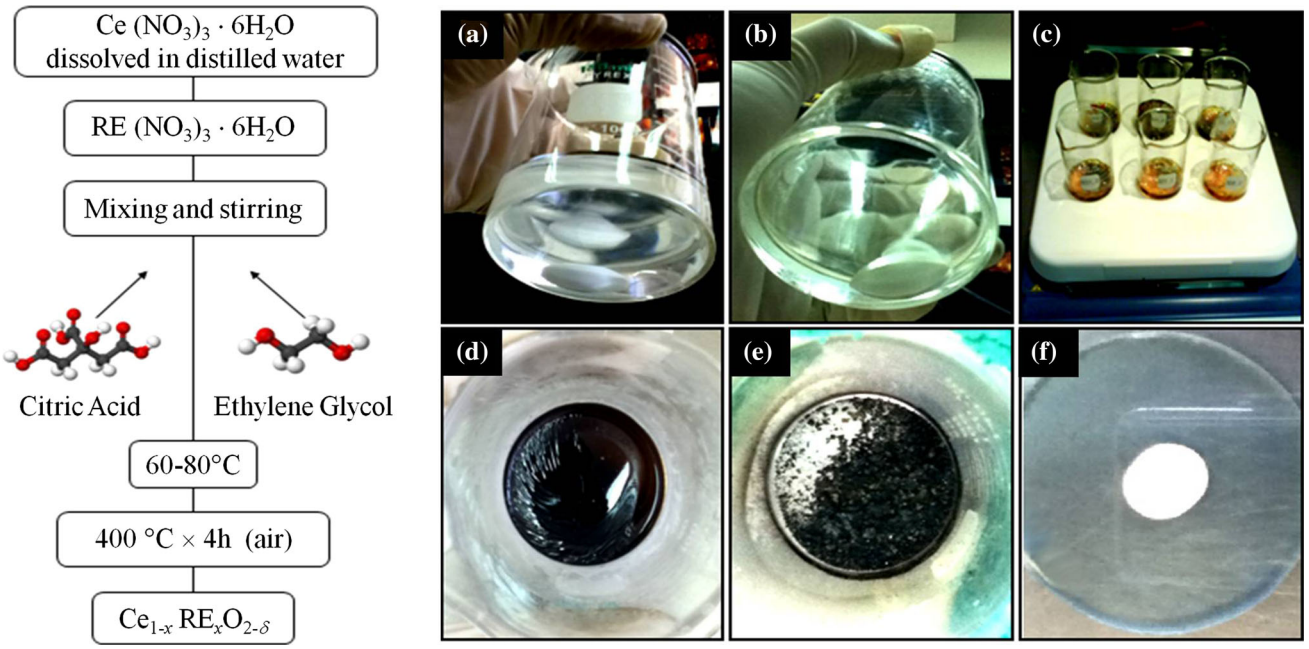

Figure 1 Flow chart of the Pechini method and synthesis process: **a** sol, **b** gel, **c** solid solutions, **d** resin, **e** carbonization, and **f** nanostructured powder after carbonization at 400 °C for 4 h in air atmosphere.

temperature. For this homogeneous solution, the molar ratio of citric acid and oxide was 5:1. pH was further stabilized at neutral, resulting in a light yellow solution. Ethylene glycol was added until the solution became homogeneous and transparent. To increase the homogeneity of the gel, it is necessary to add an adequate quantity of citric acid, which stabilizes the chelated complexes, and ethylene glycol, which prevents agglomerated compounds. Stirring on a hot plate continued for 12 h at a temperature between 60 and 80 °C. A resin is gradually formed. As part of the exothermic process of polymerization, NO_x and water vapor were released. After polymerization and evaporation, temperature was increased to 300 °C for 12 h to dry the resin and decompose the volatile organic compounds, leading to polymeric breakdown and carbonization. A further calcination treatment was applied in a furnace under air atmosphere in two steps: 1 h at 110 °C, immediately followed by 4 h at 400 °C, and the compound was left to cool until it reached room temperature. Homogeneous nanostructured powders were obtained. Figure 1 shows a diagram of the preparation process, along with photographs of the synthesis steps used to obtain the compounds.

Materials characterizations

Synthesized compounds were analyzed by X-ray diffraction (XRD) to check the phase formation and to determine the structure of all compounds, using an X-ray Bruker D-8 Advance diffractometer with $Cu_{K\alpha 1}$ radiation ($\lambda = 1.54056$ Å), 30 kV and 40 mA, with a secondary monochromator. Data were collected at room temperature from 20° to 130° 2θ°, with steps of 0.008° and 1 s/step; sample was spinning at 30 rev min^{-1}. Whole pattern fitting (Rietveld refinement) was calculated to determine the variation of lattice parameters as a function of Gd or Sm contents. Powders were pelleted at 1 ton with an initial diameter ϕ of 12.7–12.9 mm and thickness between 0.7 and 0.9 mm. A further sintering step was taken at 1450 °C for 6 h; after this step, pellet dimensions were in the range of $\phi = 8.9$–9.4 mm and 0.6–0.8 mm of thickness. Phase identification was carried out using the EVA software by Bruker. To analyze the kinematics of the reaction, thermogravimetric analyses (TGA) and differential scanning calorimetry (DSC) measurements were carried out with a TA Instruments SDT Q600 analyzer. Precursor resins with initial weights between 30 and 50 mg were heated from 25–1000 °C at 10 °C/min in air atmosphere; powder samples of synthesized compounds (400 °C), with initial weights between 2 and 5 mg, were heated in the same range of temperatures, both under air and N_2 atmospheres. Results were analyzed with the Universal Analysis 2000 software, TA Instruments. BET measurements were carried out by

nitrogen adsorption with a SORP MINI II equipment from BEL Japan, Inc. Initial weights of the samples were between 0.1 and 0.3 g. Results were analyzed using the BEL Master software.

Previous to morphological studies, the pelleted samples were heated at 80 °C overnight and then cleaned under Ar pressured flux. The morphology and elemental composition of all compounds were studied by scanning electron microscopy (SEM) and energy dispersive X-ray spectroscopy (EDS), respectively, using a JEOL 7600F electron microscope. Additional morphological studies by atomic force microscopy (AFM) and high-resolution transmission electron microscopy (HRTEM) were carried out. For AFM analysis, a JEOL JSPM-421 SPM microscope was used. Results were analyzed using the software WinSPM DPD version 2.0 by JEOL. For HRTEM studies of powder dried doped-ceria, the samples were placed on Cu grids (300 mesh) which were previously covered in-house in a Butvar B-98 thin film, followed by a carbon film. The equipment used was a TITAN FEI electron microscope, 300 kV, with a resolution of 0.085 nm.

Conductivity measurements

A Solartron SI 1260 Impedance/Gain-phase analyzer, connected in series with a Solartron 1296 dielectric interphase, was used to analyze the transport properties in the range of frequencies 10^{-2} to 10^{7} Hz, with an applied voltage of 100 mV and 10 points per decade. AC impedance measurements were taken from dense pellets (sintered at 1450 °C), which were coated on both sides with Au tincture, as a function of temperature between 200 and 750 °C in air using a Thermolyne 47900 furnace with a two terminal jig. Impedance diagrams were fitted using the ZView software by Scribner Associates.

Results and discussion

XRD analysis

X-ray diffraction patterns showed that all the samples are cubic fluorite single-phase structures (ICDD file 04–013–4361, cubic fluorite structure of ceria), which correspond to space group $Fm\bar{3}m$ (225), with cations at the 4(a) sites at 0,0,0 and the oxygen atoms at the 8(c) sites ¼, ¼, ¼ [37]. Figure 2a, b shows the collected XRD data for all doped and undoped ceria samples investigated. Compounds $Ce_{0.85}Gd_{0.15}O_{1.925}$, $Ce_{0.80}Gd_{0.20}O_{1.90}$ and $Ce_{0.85}Sm_{0.15}O_{1.925}$, $Ce_{0.80}Sm_{0.20}O_{1.90}$ will be referred as G15, G20 and S15, S20, respectively.

In order to examine the lattice parameter variation more accurately, a Rietveld refinement was carried out on the XRD data of all solid solutions. Figure 2c, d shows the collected XRD data and the fitted curves for the solid solutions G20 and S20, respectively. Figure 2e, f shows the relative lattice distortion consistent with ionic radii. Table 1 shows the results of the performed structural analysis. From the refinement we can conclude that the lattice parameter "*a*" evolves linearly as a function of the content of Sm or Gd in the CeO_2 cell; such behavior follows Vegard's law. The expansion of the unit cell parameters compared to those of undoped ceria is a consequence of the ionic radius difference: Sm^{3+}(1.079 Å) > Gd^{3+}(1.053 Å) > Ce^{4+}(0.970 Å) [38]; the substitution of Ce^{4+} with Sm^{3+} and Gd^{3+} in the lattice of CeO_2 enlarges the crystal lattice.

The nanometric size of the synthesized powders was evidenced by diffraction peak broadening. The average crystallite sizes D_{XRD} were calculated from the full width half maximum (FWHM) of the (2 2 0) reflections by using the modified Debye–Scherrer equation [39] and Rietveld refinement [40]. Crystallite sizes obtained are in the range of 5–11 nm.

DSC–TGA analyses

Thermal decomposition of the precursor resins was investigated in a dry air atmosphere by simultaneous DSC–TGA. Figure 3a shows the DSC–TGA curve of G20 sample. From the DSC plot, two endothermic peaks were observed, centered at 87 and 195 °C, which correspond to the two stages of weight loss, as shown in the TGA curve. Although the first endothermic peak corresponds to loss of moisture in the sample, the second endothermic peak may be due to further water loss, but mainly due to the decomposition of nitrates and the expelling of different volatile organic compounds, i.e., NO_x, CO, and CO_2, with a considerable total weight loss of ~82 %. Also, one shallow and one large exothermic peak are observed at 300 and 402 °C, respectively. The large peak showing a weight loss of ~11 % is due to an autoignition process of the ethylene glycol polymerized with the metallic ions of the resin. On heating

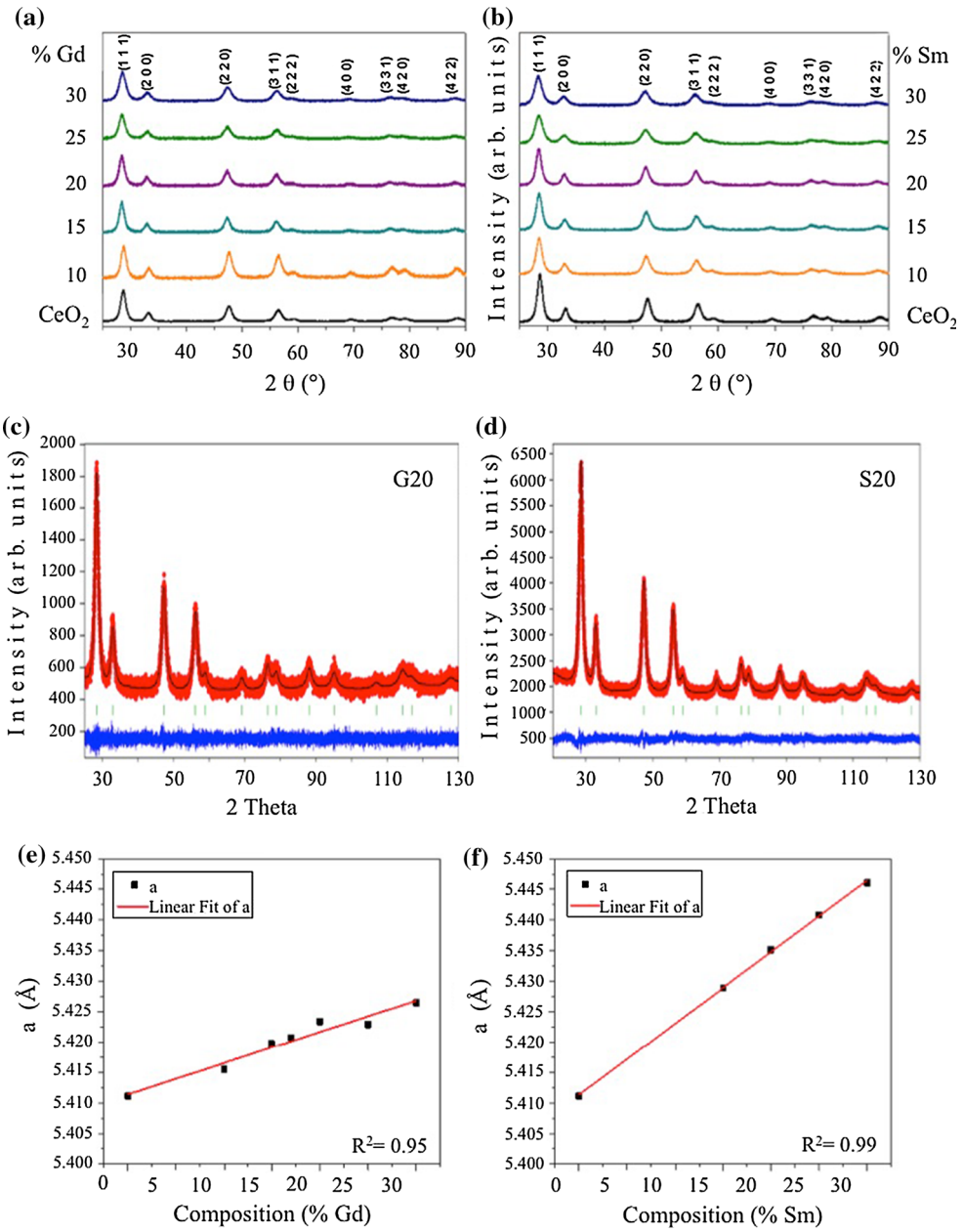

Figure 2 XRD patterns of ceria-doped compounds with: **a** Gd and **b** Sm, both heated at 400 °C for 4 h. Rietveld refinement from selected samples: **c** G20 and **d** S20. Lattice parameter as a function of dopant content: **e** Gd and **f** Sm.

Table 1 Unit cell parameters and *R*-factors, obtained from Rietveld refinement of the XRD patterns of samples heated at 400 °C for 4 h

Sample (400 °C, 4 h)	*a* (Å)	Crystallite size $_{(Rietveld)}$ (nm)	χ^2	Bragg R-factor	RF-factor
CeO_2	5.4111	6	1.55	2.55	1.52
$Ce_{0.85}Gd_{0.15}O_{1.925}$ (G15)	5.4197	5	1.03	1.45	1.35
$Ce_{0.80}Gd_{0.20}O_{1.90}$ (G20)	5.4234	5	1.03	1.59	1.44
$Ce_{0.85}Sm_{0.15}O_{1.925}$ (S15)	5.4290	5	1.31	2.33	1.62
$Ce_{0.80}Sm_{0.20}O_{1.90}$ (S20)	5.4351	5	1.28	2.50	1.72

Number of space group: 225, Hermann–Mauguin symbol: Fm-3m, crystal system: cubic, general multiplicity: 192

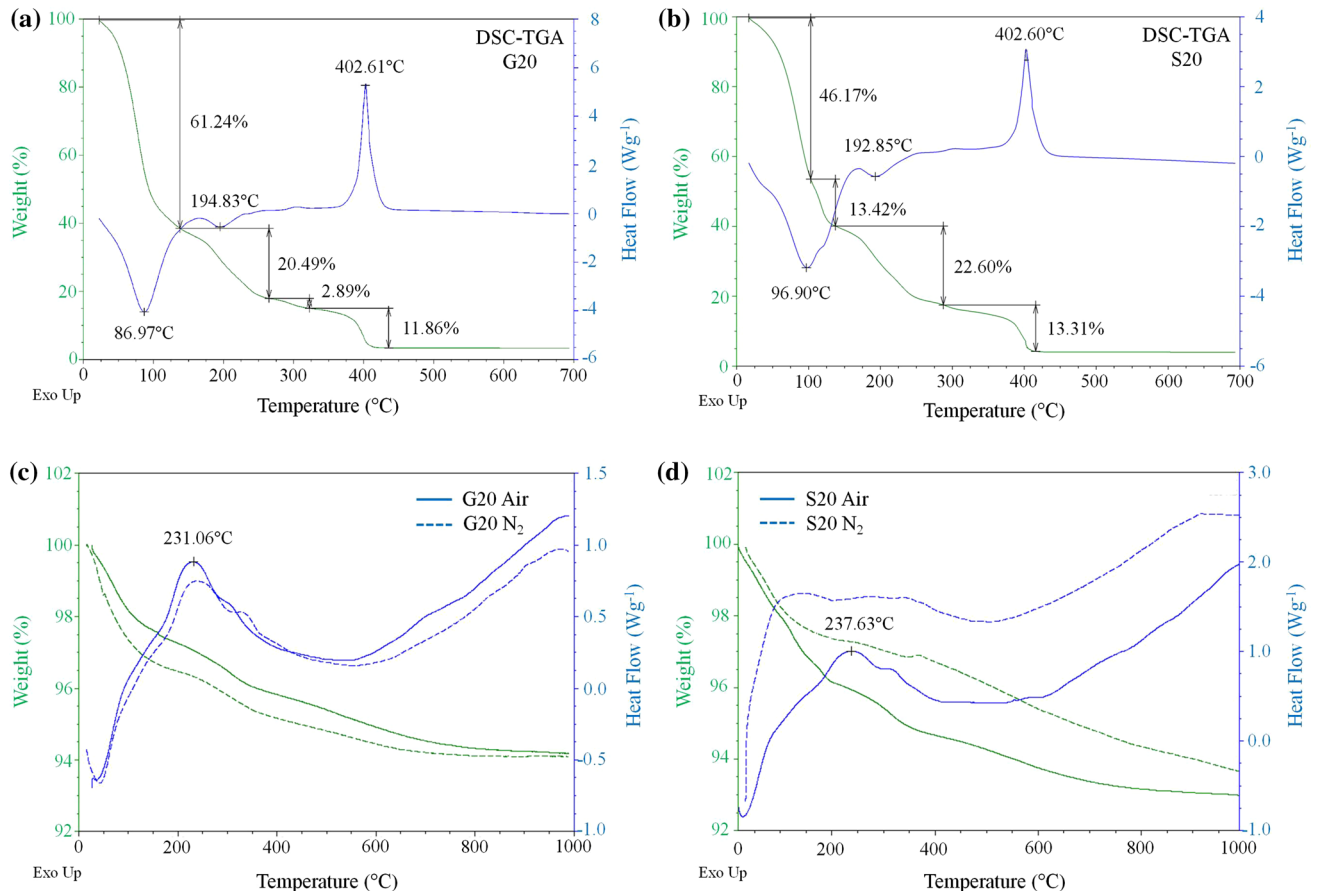

Figure 3 DSC–TGA graphs of **a** G20 and **b** S20 precursor resin in air and **c** G20, **d** S20 synthesized powder samples under air/N_2 atmospheres.

above 410 °C, the weight value remains constant as well as the DSC curve, showing that the synthesis process has ended, and a final product has been obtained. Figure 3b shows an analogous behavior for the S20 sample. These results are consistent with those reported by Arabacıa et al. [41] and Mercadelli *et al.* [42] who observed that the syntheses for similar compounds were completed around 400 °C. Figure 3c, d shows the DSC–TGA plots under air and N_2 atmospheres for the solid solutions G20 and S20 synthetized at 400 °C, in which we observe a low temperature weight loss (∼1–2 %) corresponding to the adsorbed water, and a second weight loss (∼4–5 %) related to the thermal dehydration of the hydrous gadolinium/samaria-doped ceria around 200–400 °C, observing total dehydration of the compounds until 700–800 °C for both samples. DSC–TGA results suggested the heating and cooling rates for both synthesis and sintering processes to control the microstructure and to obtain the optimal densification.

BET measurements

For materials used as electrolytes, the surface area, mean pore diameter, and particle size are all important properties, since these materials should be dense (non-porous) and with a high area-to-volume ratio to avoid short circuit and/or combustion processes. Nitrogen adsorption was determined for all samples synthesized (G15, G20, S15, and S20). Figure 4a, b shows BET plots for Gd- and Sm-doped ceria, with corresponding sorption isotherms. Based on IUPAC classification, the obtained N_2 adsorption/desorption isotherms (type II) may be associated with non-porous or macro-porous materials (pore size >50 nm) [43]. To identify the nature of these materials, BET results indicated that the mean pore diameter for all samples is between 3 and 5 nm, so it can be concluded that all samples are non-porous materials. Table 2 shows the data derived from BET results.

In this work, the resulting specific surface area values for G15, G20, S15, and S20 samples are

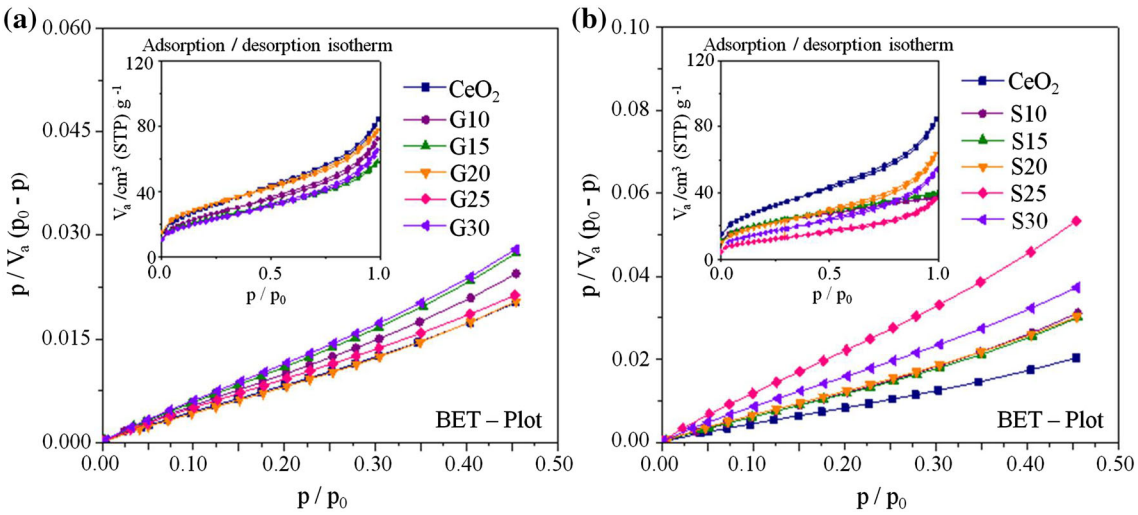

Figure 4 Doped ceria BET plots with adsorption/desorption isotherms in inset, for compounds **a** Gd and **b** Sm, synthesized at 400 °C.

Table 2 BET measurements of G15, G20, S15, and S20 samples heated at 400 °C for 4 h

Sample (400 °C, 4 h)	$a_{s\ (BET)}$ (m^2g^{-1})	Mean pore diameter (nm)	V_m (cm^3g^{-1})	Particle Size $_{(BET)}$ (nm)
CeO_2	86.3	4	25.2	10
$Ce_{0.85}Gd_{0.15}O_{1.925}$ (G15)	82.4	4	18.9	10
$Ce_{0.80}Gd_{0.20}O_{1.90}$ (G20)	110.7	4	25.4	7
$Ce_{0.85}Sm_{0.15}O_{1.925}$ (S15)	77.4	3	17.8	10
$Ce_{0.80}Sm_{0.20}O_{1.90}$ (S20)	74.6	5	17.1	11

between 75 and 110 m^2g^{-1}, which are greater than the uppermost values previously reported; for G15 49.4 [44] and 97.6 m^2g^{-1} [31], for G20 35.9 m^2g^{-1} [45], and for S15 89.2 m^2g^{-1} [31]. This holds even for compounds of doped ceria synthesized by sol–gel, 73 m^2g^{-1} [46].

From specific surface area values, particle sizes D_{BET} were calculated using the following equation [47]:

$$D_{BET} = \frac{6}{a_{S(BET)\cdot\rho th}}, \quad (2)$$

where $a_{s(BET)}$ is the surface area of the powder and ρ_{th} the theoretical densities of the samples, obtained by [48]:

$$\rho th = \frac{FW \times Z}{N_A \times V}. \quad (3)$$

The theoretical densities are thus 7.21 gcm^{-3} for CeO_2, 7.23 gcm^{-3} for G15, 7.24 gcm^{-3} for G20, 7.17 gcm^{-3} for S15, and 7.15 gcm^{-3} for S20. With these values and Eq. 2, particle sizes of 10 nm for CeO_2, 10 nm for G15, 8 nm for G20, 11 nm for S15, and 11 nm for S20 were determined.

SEM–EDS analyses

In electrolytes for IT-SOFCs, microstructures with small grain sizes are preferred, to provide high mechanical stability, and good densification to avoid gas percolation. Micrographs show soft-agglomerated nanometric powders with good homogeneity. Figure 5a shows that the nanometric nature of the samples led to strong interactions among them, producing the formation of particle agglomerates, which reduces the superficial energy. From EDS results, obtained from global and punctual measurements, the stoichiometry values for each compound were calculated, which are in good agreement with the nominal values.

Electrolytes in SOFCs should be dense, to avoid contact between combustible and oxidant gases. To obtain dense samples from the sintering process, it is favorable if the starting products are nanometric

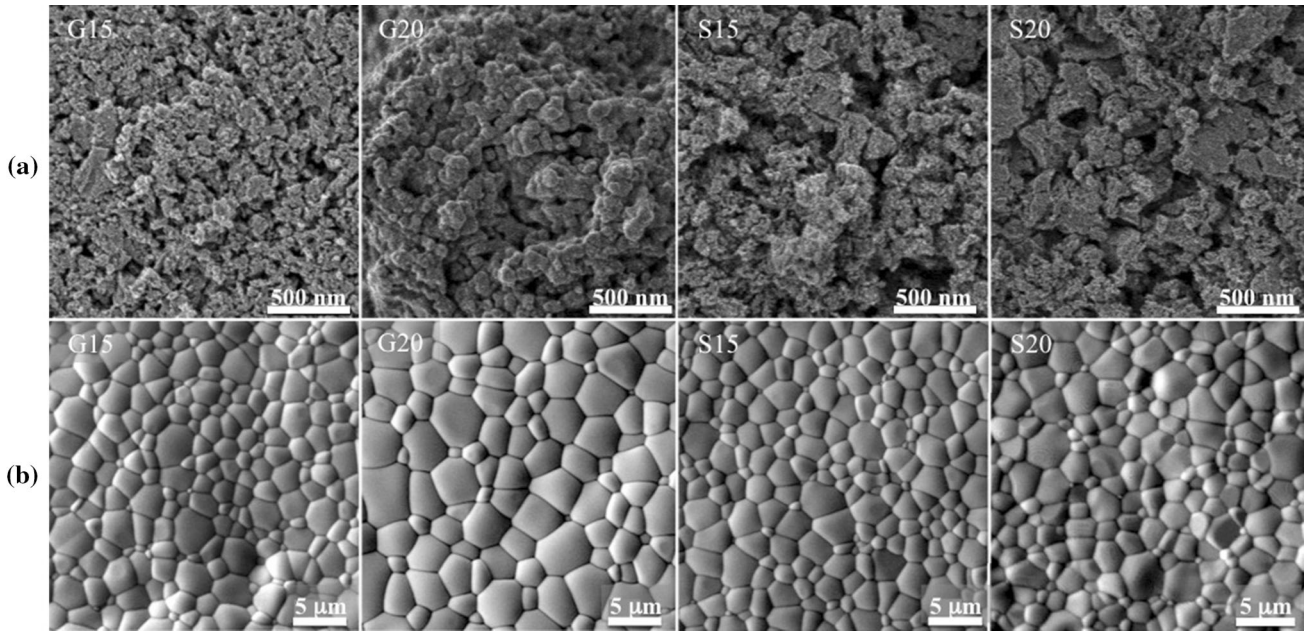

Figure 5 SEM micrographs for G15, G20, S15, and S20, heated at **a** 400 °C for 4 h and **b** 1450 °C for 6 h.

monodispersed powders. Factors such as particle size and shape, as well as agglomeration, play an important role in the sinterability of $Ce_{1-x}RE_xO_{2-\delta}$ powders [6]. To accomplish this goal, nanometric powders were placed under ultrasonication for 30 min. Powders were pelleted and heated at 1450 °C for 6 h. Figure 5b corresponds to SEM micrographs of these samples, that show high density products, with homogeneous surface and well-defined grains. The temperature for the sintering process was carefully determined to avoid stress in the samples, and heating was stopped when the grains started to show slip bands (Fig. 5b for S20).

Surface area analyses were simulated with the IJ148 software to calculate grain sizes of the samples, results are found for G15 1–3 μm and for G20, S15, and S20 1–5 μm. Also, relative densities were determined by Archimedes principle using distilled water, for G15 97 %, G20 96 %, S15 98 %, and S20 96 %.

AFM measurements

Additional morphological studies by AFM were carried out for samples as synthesized. Figure 6a shows a 3-dimensional projection of surface topographic images for G20 and S20 samples, which exhibit high surface homogeneity and good dispersion with particle agglomeration. Figure 6b shows roughness data and AFM images for G15 and S15 samples, pelleted ($\phi = 7$ mm) and thermally treated at 400 °C, obtained using WinSPM DPS software V 2.0. Results show that the average roughness values, *Ra*, for the samples are under 1 nm, *e.g.*, $Ra_{G15} = 0.56$ nm and $Ra_{S15} = 0.47$ nm, this low roughness implies a high surface homogeneity. Also, the decrease in surface roughness was found to lower the ohmic resistance of SOFCs, which indicates that the ion conduction mainly occurs along the electrolyte surface or at a near-surface depth of the electrolyte [49]; specialized geometric designs could be created to take advantage of this and improve the conductivity in the final device. Nanometric particle sizes in the range of 7–10 nm were observed for all compounds, as shown in Table 3.

HRTEM analysis

HRTEM was used to observe the grain size and crystal structure of samples as synthesized. Figures 7a, b correspond to the selected area electron diffraction (SAED) patterns for samples G15 and S15, respectively, and these display the characteristic concentric rings, which correspond to a large number of crystals diffracting at the same time. Micrographs showed agglomerates of nanocrystals, with sizes in the range of 5–10 nm (Table 3). The sizes are a match with those determined by the use of XRD. Interatomic distances were used to determine some crystal

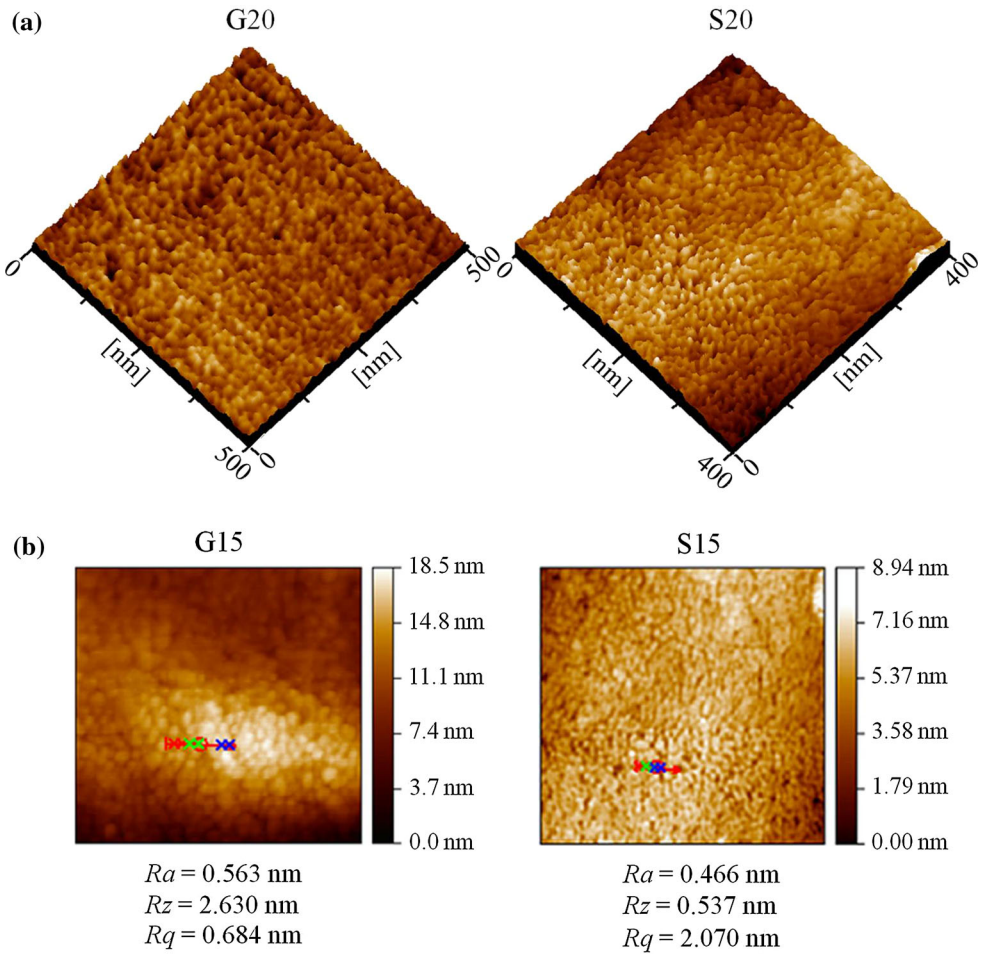

Figure 6 **a** AFM 3D–projection of G20 and S20 samples and **b** roughness data and AFM images for G15 and S15 samples after heating at 400 °C for 4 h.

Table 3 Comparison of crystallite and particle sizes obtained by XRD (Scherrer), HRTEM, SEM, and AFM techniques, for samples heated at 400 °C for 4 h

Sample (400 °C, 4 h)	Crystallite size (nm)		Particle size (nm)	
	XRD Scherrer	HRTEM	SEM	AFM
CeO_2	11	8–10	5–10	7–10
$Ce_{0.85}Gd_{0.15}O_{1.925}$ (G15)	10	5–10	10–12	7–9
$Ce_{0.80}Gd_{0.20}O_{1.90}$ (G20)	10	7–10	10–12	8–10
$Ce_{0.85}Sm_{0.15}O_{1.925}$ (S15)	10	5–9	5–10	7–9
$Ce_{0.80}Sm_{0.20}O_{1.90}$ (S20)	11	8–10	5–10	8–10

orientations, in particular $d_{111} = 3.1$ Å and $d_{200} = 2.7$ Å.

Transport properties

Impedance measurements were carried out in air, in the temperature range 200–750 °C. From 200 to 300 °C, all the plots exhibited two semicircles in the high and intermediate frequency region, with a short tail at low frequencies. Associated capacitances led to the identification of different processes; the intermediate frequency arc (10^{-7} to 10^{-8} F) corresponds to the grain boundaries, while the high frequency arc (10^{-10} to 10^{-11} F) is due to the bulk/grain, and for the low frequencies region the short tail may be ascribed to the electrode/electrolyte interface contributions. As the measurement temperature was increased from 300 to 750 °C, the contribution from the bulk/grain disappears, giving way to the contributions from the grain boundary and the electrode/electrolyte interphase (10^{-3} to 10^{-4} F); it was observed in all compounds that the conductivity

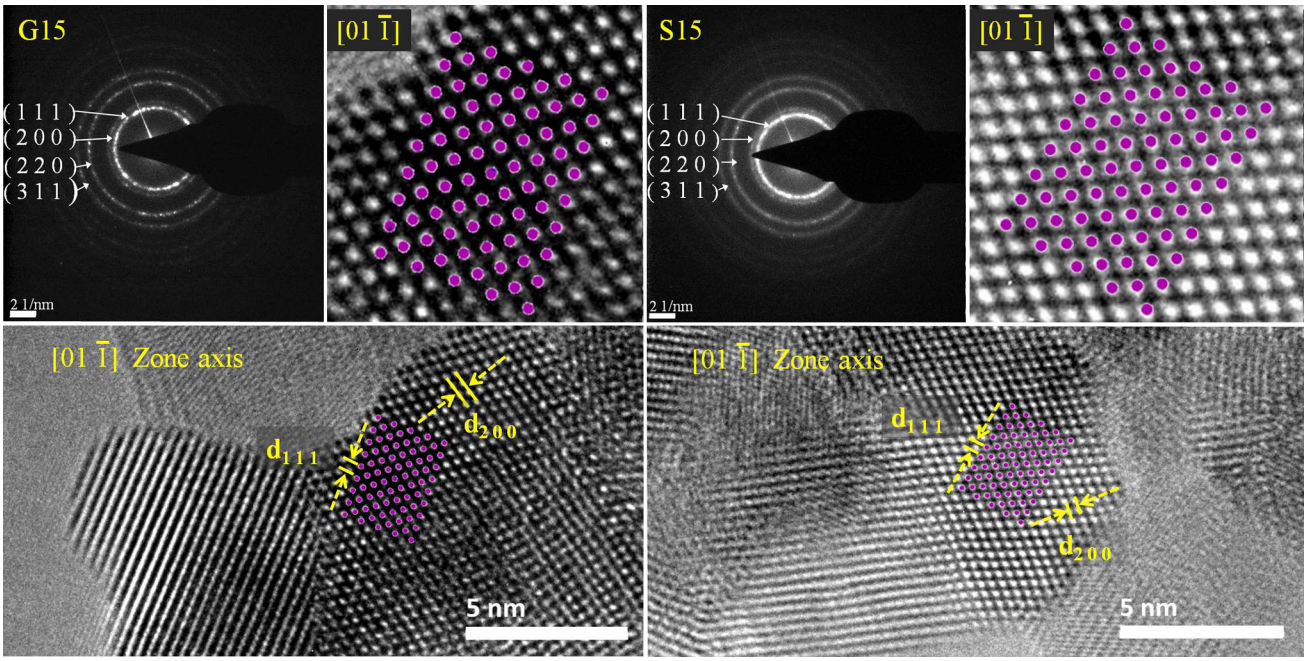

Figure 7 HRTEM micrographs, SAED patterns of: **a** G15 and **b** S15 samples heated at 400 °C for 4 h.

associated to the grain boundary dominates the conductive process. Impedance data were modeled by equivalent circuits using ZView 3.3e software; resistivity of grain and grain boundary, R_g and R_{gb}, respectively, were obtained by fitting measured impedance data with two parallel *R*-CPE elements connected in series, where CPE denotes a constant phase element. Figure 8a shows the impedance plots for G15, G20, S15, and S20 measured at 300 °C. Fitted data for S20 are shown in the inset, Figs. 8b, c, in which the contributions associated to the bulk/grain and grain boundary processes can be observed by means of plotting the impedance data as a function of temperature (Cole–Cole diagram). Figure 8d shows the total conductivity of all the samples measured at different temperatures.

Ionic and electronic conductivities are fundamentally important properties of electrolytes; ionic conductivity should be high and the electronic contribution as low as possible or even null. Addition of Gd and Sm as dopant increases the conductivity of bulk/grain and grain boundaries. In air, the main contribution on the total conductivity of ceria-based compounds is the ionic conductivity (>99.5 %), electronic conductivity being negligible [50, 51]. For different compositions of ceria-based products, reported conductivity values are $\sigma_{G15} = 4.1 \times 10^{-2}$ Scm^{-1} (700 °C) [52], $\sigma_{G20} = 5.5 \times 10^{-2}$ Scm^{-1} (800 °C) [53], $\sigma_{S15} = 2.6 \times 10^{-2}$ Scm^{-1} (550 °C) [54], and $\sigma_{S20} = 9.5 \times 10^{-2}$ Scm^{-1} (800 °C) [53]. In this work, at 600 °C, S20 sample exhibits a conductivity of 3.6×10^{-2} Scm^{-1}, one order of magnitude higher than the conductivity of G20, with 3.2×10^{-3} Scm^{-1}.

From the following relationship ($\sigma \propto R^{-1}$), the maximum conductivity for each sample can be observed when the grain boundary arc is at its minimum. For the compounds studied in this work, this occurs in the temperature range of 615–730 °C; the maximum values for conductivities are $\sigma_{G15} = 4.1 \times 10^{-1}$ Scm^{-1} (730 °C), $\sigma_{G20} = 1.3 \times 10^{-1}$ Scm^{-1} (660 °C), $\sigma_{S15} = 8.1 \times 10^{-2}$ Scm^{-1} (670 °C), and $\sigma_{S20} = 1.9 \times 10^{-1}$ Scm^{-1} (615 °C). In this temperature range, the results are up to two orders of magnitude higher than those values previously reported [55–60].

According to Kilner and Brook, maximum ionic conductivity in doped fluorite-structured oxide is observed when the lattice elastic strain is minimal; this means that the ionic radius of the dopant should be as close to r_c as possible [61]. For cerium, the lowest size mismatch is with gadolinium and samarium [62]. By increasing the dopant concentration, we heighten the ionic conductivity; however, this only occurs until a certain percentage of dopant, since the conductivity reaches a maximum value and then decreases due to the low mobility of the

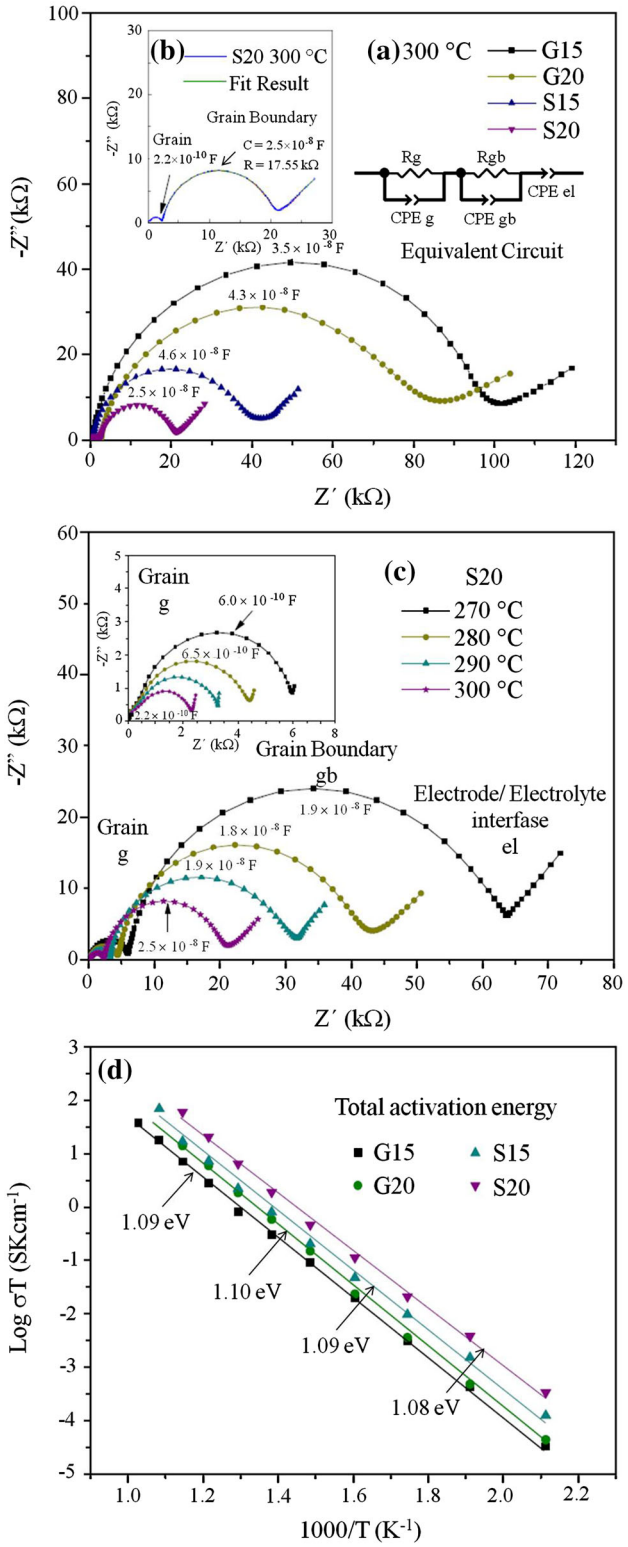

Figure 8 **a** Impedance plots for selected samples. For S20: **b** fitted data/equivalent circuit and **c** impedance plots at different temperatures. **d** Total activation energies for G15, G20, S15, and S20 samples sintered at 1450 °C for 6 h.

associated defects in the lattice [63]; in the case of doped ceria, the maximum associated ionic conductivities are observed in the range of 15–25 % doping content [56, 64]. Moreover, the addition of dopants increases the lattice parameter and therefore, the unit cell volume, which may produce a decrease in the contribution of the local strain and may facilitate the diffusion of oxygen ions through the lattice reducing the activation energy [65].

In the selected samples of this work, the total activation energy values for all the associated contribution processes (bulk/grain, grain boundary, total) are around 0.9–1.1 eV. Although the activation energies were in the range previously reported [31, 53, 54, 56, 66–70], conductivities were obtained at intermediate temperatures (500–730 °C), which are due not only to the microstructure and high homogeneity of the products but also to the good densification; this is a direct result of the controlled synthesis process.

Conclusion

High-purity nanopowders of $Ce_{1-x}RE_xO_{2-\delta}$ (RE = Sm, Gd, with $0 \leq x \leq 0.30$) were synthesized by the Pechini method at 400 °C. XRD results showed single-phase compounds with a stable cubic fluorite structure in the temperature interval of 400–1450 °C. The width of all XRD peaks, along with HRTEM images indicated nanometric materials with crystallite sizes between 5 and 11 nm, in good agreement with values obtained by BET, SEM, and AFM particle sizes. The specific surface area values of the compounds are among the largest reported for synthesis carried out in air. The reduction in particle size, mesoporosity, and homogeneity in the compounds maximized the effectiveness of the densification process, leading to dense pellets which will diminish issues due to spontaneous short circuit or combustion when the material is used as an electrolyte in a SOFC. Transport properties were observed in the temperature range of 200–750 °C, where the main conduction mechanism is due to grain boundary processes. Conductivity values in the order of 10^{-1} Scm^{-1}, at measurement temperatures in the range of 600–730 °C, were found to be comparable with the highest values reported in the literature for similar compounds, but at temperatures over 800 °C, thus

achieving a reduction in the operating temperature of these types of electrolytes.

Acknowledgements

PERA (175598) thanks CONACyT for grant 203342. The authors gratefully thank D. Cabrero, O. Novelo, J. Romero, H. Pfeiffer (all at the IIM), and A. Ponce (CICATA) for technical assistance and acknowledge PAPIIT-UNAM (IN119010) and CONACyT (ECOS-M13P01) projects for financial support.

Compliance with ethical standards

Conflict of interest The authors declare that they have no conflict of interest.

References

[1] Steele BCH, Heinzel A (2001) Materials for fuel-cell technologies. Nature 414:345–352. doi:10.1038/35104620

[2] Haile SM (2003) Fuel cell materials and components. Acta Mater 51:5981–6000. doi:10.1016/j.actamat.2003.08.004

[3] Dokiya Masayuki (2002) SOFC system and technology. Solid State Ionics 152–153:383–392. doi:10.1016/S0167-2738(02)00345-4

[4] Neelima M, Amitava B, Alka G, Shobit O, Kantesh B (2015) Progress in material selection for solid oxide fuel cell technology: a review. Prog Mater Sci 72:141–337. doi:10.1016/j.pmatsci.2015.01.001

[5] O'Hayre R, Cha SW, Colella W, Prinz FB (2009) Fuel cell fundamentals, 2nd edn. Willey, New York. ISBN 978-0-470-25843-9

[6] Shao Z, Zhou W, Zhu Z (2012) Advanced synthesis of materials for intermediate-temperature solid oxide fuel cells. Prog Mater Sci 57:804–874. doi:10.1016/j.pmatsci.2011.08.002

[7] Fergus JW (2006) Electrolytes for solid oxide fuel cells. J Power Sources 162:30–40. doi:10.1016/j.jpowsour.2006.06.062

[8] Jaiswal N, Gupta B, Kumar D, Parkash O (2015) Effect of addition of erbium stabilized bismuth oxide on the conductivity of lanthanum doped ceria solid electrolyte for IT-SOFCs. J Alloys Compd 633:174–182. doi:10.1016/j.jallcom.2014.12.243

[9] Hirano M, Inagaki M, Mizutani Y, Nomura K, Kawai M, Nakamura Y (2000) Mechanical and electrical properties of Sc_2O_3-doped zirconia ceramics improved by post sintering with HIP. Solid State Ionics 133:1–9. doi:10.1016/S0167-2738(00)00706-2

[10] Mizutani Y, Tamura M, Kawai M, Yamamoto O (1994) Development of high-performance electrolyte in SOFC. Solid State Ionics 72(2):271–275. doi:10.1016/0167-2738(94)90158-9

[11] Tietz F (1999) Thermal expansion of SOFC materials. Ionics 5:129–139. doi:10.1007/BF02375916

[12] Muccillo R, Buissa Netto RC, Muccillo ENS (2001) Synthesis and characterization of calcia fully stabilized zirconia solid electrolytes. Mater Lett 49(3–4):197–201. doi:10.1016/S0167-577X(00)00367-0

[13] Stevenson JW, Hasinska K, Canfield NL, Armstrong TR (2000) Influence of cobalt and iron additions on the electrical and thermal properties of (La, Sr)(Ga, Mg)$O_{3-\delta}$. J Electrochem Soc 147(9):3213–3218. doi:10.1149/1.1393885

[14] Lybye D, Poulsen FW, Mogensen M (2000) Conductivity of A- and B-site doped $LaAlO_3$, $LaGaO_3$, $LaScO_3$ and $LaInO_3$ perovskites. Solid State Ionics 128:91–103. doi:10.1016/S0167-2738(99)00337-9

[15] Nguyen TL, Dokiya M (2000) Electrical conductivity, thermal expansion and reaction of (La, Sr)(Ga, Mg)O_3 and (La, Sr)AlO_3 system. Solid State Ionics 132:217–226. doi:10.1016/S0167-2738(00)00661-5

[16] Zhang TS, Ma J, Cheng H, Chan SH (2006) Ionic conductivity of high-purity Gd-doped ceria solid solutions. Mater Res Bull 41(3):563–568. doi:10.1016/j.materresbull.2005.09.008

[17] Kharton VV, Figueiredo FM, Navarro L, Naumovich EN, Kovalevsky AV, Yaremchenko AA, Viskup AP, Carneiro A, Marques FMB, Frade JR (2001) Ceria-based materials for solid oxide fuel cells. J Mater Sci 36(5):1105–1117. doi:10.1023/A:1004817506146

[18] Mogensen M, Lindegaard T, Hansen UR, Mogensen G (1994) Physical properties of mixed conductor solid oxide fuel cell anodes of doped CeO_2. J Electrochem Soc 141(8):2122–2128. doi:10.1149/1.2055072

[19] Herle JV, Horita T, Kawada T, Sakai N, Yokokawa H, Dokiya M (1996) Low temperature fabrication of (Y, Gd, Sm)-doped ceria electrolyte. Solid State Ionics 86–88:1255–1258. doi:10.1016/0167-2738(96)00297-4

[21] Xu H, Yan H, Chen Z (2006) Sintering and electrical properties of $Ce_{0.8}Y_{0.2}O_{1.9}$ powders prepared by citric acid-nitrate low temperature combustion process. J Power Sources 163(1):409–414. doi:10.1016/j.jpowsour.2006.09.021

[22] Zhu B (1999) Fast ionic conducting film ceramic membranes with advanced applications. Solid State Ionics 119:305–310. doi:10.1016/S0167-2738(98)00519-0

[23] Gerhardt-Anderson R, Nowick AS (1981) Ionic conductivity of CeO_2 with trivalent dopants of different ionic radii. Solid State Ionics 5:547–550. doi:10.1016/0167-2738(81)90313-1

[24] Kilner JA (1983) Fast anion transport in solids. Solid State Ionics 8:201–207. doi:10.1016/0167-2738(83)90017-6

[25] Eguchi K, Setoguchi T, Inoue HA (1992) Electrical properties of ceria-based oxides and their application to solid oxide fuel cells. Solid State Ionics 52:165–172. doi:10.1016/0167-2738(92)90102-U

[26] Keshmiri M, Kesler O (2006) Colloidal formation of monodisperse YSZ spheres: kinetics of nucleation and growth. Acta Mater 54(16):4149–4157. doi:10.1016/j.actamat.2006.05.010

[27] Nualpang W, Laosiripojana N, Assabumrungrat S, Injarean U, Pichestapong P, Charojrochkul S (2008) Combustion synthesis of $Ce_{0.9}Gd_{0.1}O_{1.95}$ for use as an electrolyte for SOFCs. J Metals Mater Miner 18(2):223–227. doi: 10.1016/j.jallcom.2012.06.036. http://www.material.chula.ac.th/Journal/v18-2-2/223-227%20NUALPANG.pdf

[28] Terribile D, Trovarelli A, Leitenburg C, Dolcetti G (1997) Unusual oxygen storage/redox behavior of high-surface-area ceria prepared by a surfactant-assisted route. J Chem Mater 9:2676–2678. doi:10.1021/cm9702732

[29] Ishihara T, Kilner JA, Honda M, Sakai N, Yokokawa H, Takita Y (1998) Oxygen surface exchange and diffusion in $LaGaO_3$ based perovskite type oxides. Solid State Ionics 113:593–600. doi:10.1016/S0167-2738(98)00390-7

[30] Kaneko K, Inoke K, Freitag B, Hungria AB, Midgley Paul A, Hansen TW, Zhang J, Ohara S, Adschiri T (2007) Structural and morphological characterization of cerium oxide nanocrystals prepared by hydrothermal synthesis. Nano Lett 7(2):421–425. doi:10.1021/nl062677b

[31] Prado-Gonjal J, Schmidt R, Espindola-Canuto J, Ramos-Alvarez P, Moran E (2012) Increased ionic conductivity in microwave hydrothermally synthesized rare-earth doped ceria $Ce_{1-x}RE_xO_{2-(x/2)}$. J Power Sources 209:163–171. doi:10.1016/j.jpowsour.2012.02.082

[32] Song X, Jiang N, Li Y, Xu D, Qiu G (2007) Synthesis and Characterization of Y-doped mesoporous CeO_2 using a chemical precipitation method. J Rare Earths 25:428–433. doi:10.1016/S1002-0721(07)60450-5

[33] Lapa CM, Figueiredo FM, De Souza DPF, Song L, Zhu B, Marques FMB (2010) Synthesis and characterization of composite electrolytes based on samaria-doped ceria and Na/Li carbonates. Int J Hydrog Energy 35:2953–2957. doi:10.1016/j.ijhydene.2009.05.036

[34] Pérez-Coll D, Núñez P, Frade JR, Abrantes JCC (2003) Conductivity of CGO and CSO ceramics obtained from freeze-dried precursors. Electrochim Acta 48(11):1551–1557. doi:10.1016/S0013-4686(03)00027-6

[35] Laberty-Robert C, Long JW, Lucas EM, Pettigrew KA, Stroud RM, Doescher MS, Rolison DR (2006) Sol–Gel-derived ceria nanoarchitectures: synthesis, characterization, and electrical properties. Chem Mater 18(1):50–58. doi:10.1021/cm051385t

[36] Fuentes RO, Baker RT (2008) Synthesis and properties of Gadolinium-doped ceria solid solutions for IT-SOFC electrolytes. Int J Hydrog Energy 33:3480–3484. doi:10.1016/j.ijhydene.2007.10.026

[37] Varez A, Garcia Gonzalez E, Sanz JJ (2006) Cation miscibility in CeO_2–ZrO_2 Oxides with fluorite structure A combined TEM, SAED and XRD Rietveld analysis. Mater Chem 16:4249–4256. doi:10.1039/B607778A

[38] Shannon RD (1976) Revised effective ionic radii and systematic studies of interatomic distances in halides and chalcogenides. Acta Cryst A32:751–767. doi:10.1107/S0567739476001551

[39] Mikrajuddin A, Khairurrijal (2008) Derivation of Scherrer relation using an approach in basic physics course. J Nano Saintek 1(1):28–32. ISSN: 1979-0880

[40] Gonzalez G, Braham C, Lebrun JL, Chastel Y, Seiler W, Figueroa IA (2012) Microstructure and texture of Al_2Si_xSn ($x = 0$, 4, 8%) alloys processed by equal channel angular pressing. Mater Trans 53(7):1234–1239. doi:10.2320/matertrans.M2012011

[41] Arabacıa A, Öksüzömer MF (2012) Preparation and characterization of 10 mol% Gd doped CeO_2 (GDC) electrolyte for SOFC applications. Ceram Int 38:6509–6515. doi:10.1016/j.ceramint.2012.05.030

[42] Mercadelli E, Ghetti G, Sanson A, Bonelli R, Albonetti S (2013) Synthesis of CeO_2 nano–aggregates of complex morphology. Ceram Int 39:629–634. doi:10.1016/j.ceramint.2012.06.074

[43] Rouquerol J, Avnir D, Fairbridge CW, Everett DH, Haynes JM, Pernicone N, Ramsay JDF, Sing KSW, Unge KK (1994) Recommendations for the characterization of porous solids. Pure Appl Chem 66(8):1739–1758. doi:10.1351/pac199466081739

[44] Mahata T, Das G, Mishra RK, Sharma BP (2005) Combustion synthesis of gadolinia doped ceria powder. J Alloys Compd 391:129–135. doi:10.1016/j.jallcom.2004.07.085

[45] Matovic B, Boškovic S, Lj Zivkovic, Vlajic M, Krstic V (2005) Lattice parameters of Gd-doped ceria electrolytes. Mater Sci Forum 494:175–179

[46] Pavasupree S, Suzuki Y, Pivsa-Art S, Yoshikawa S (2005) Preparation and characterization of mesoporous MO_2 (M = Ti, Ce, Zr, and Hf) nanopowders by a modified sol–gel method. Ceram Int 31:959–963. doi:10.1016/j.ceramint.2004.10.009

[47] Gil V, Tartaj J, Moure C (2009) Low temperature synthesis and sintering behavior of Gd-doped ceria nanosized powders: comparison between two synthesis procedures. Bol Soc Esp Ceram V 48(2):69–76. http://boletines.secv.es/upload/20090414132803.20094869.pdf

[48] West AR (1985) Solid state chemistry and its applications. Willey, New York, pp 142. ISBN: 978–0–471–90874–6

[49] Hibino T, Hashimoto A, Suzuki M, Yano M, Yoshida SI, Sano M (2002) A solid oxide fuel cell with a novel geometry that eliminates the need for preparing a thin electrolyte film. J Electrochem Soc 149:A195–A200. doi:10.1149/1.1431573

[50] Inaba H, Tagawa H (1996) Ceria-based solid electrolyte. Solid State Ionics 83:1–16. doi:10.1016/0167-2738(95)00229-4

[51] Christie GM, Van Berkel FPF (1996) Microstructure and ionic conductivity relationships in ceria-gadolinia electrolytes. Solid State Ionics 83:17–27. doi:10.1016/0167-27389500155-7

[52] Zhang TS, Ma J, Cheng H, Chan SH (2006) Ionic conductivity of high-purity Gd-doped ceria solid solutions. Mater Res Bull 41:563–568. doi:10.1016/j.materresbull.2005.09.008

[53] Mogensen M, Sammes NM, Thompsett GA (2000) Physical, chemical and electrochemical properties of pure and doped ceria. Solid State Ionics 129:63–94. doi:10.1016/S0167-2738(99)00318-5

[54] Acharya SA, Gaikwad VM, D'Souza SW, Barman SR (2014) Gd/Sm dopant-modified oxidation state and defect generation in nano-ceria. Solid State Ionics 260:21–29. doi:10.1016/j.ssi.2014.03.008

[55] Alvarado-Flores J, Ávalos-Rodríguez L (2013) Materiales para ánodos, cátodos y electrolitos utilizados en celdas de combustible de óxido sólido (SOFC). Rev Mex Fis 59:66–87. ISSN: 0035–001X

[56] Steele BCH (2000) Appraisal of $Ce_{1-y}Gd_yO_{2-y/2}$ electrolytes for IT–SOFC operation at 500°C. Solid State Ionics 129:95–110. doi:10.1016/S0167-2738(99)00319-7

[57] Chen M, Kim BH, Xu Q, Ahn BK, Kang WJ, Huang D (2009) Synthesis and electrical properties of $Ce_{0.8}Sm_{0.2}O_{1.9}$ ceramics for IT-SOFC electrolytes by urea–combustion technique. Ceram Int 35:1335–1343. doi:10.1016/j.ceramint.2008.06.014

[58] Yao HC, Zhao XL, Chen X, Wang JC, Ge QQ, Wang JS, Li ZJ (2012) Processing and characterization of CoO and Sm_2O_3 codoped ceria solid solution electrolyte. J Power Sources 205:180–187. doi:10.1016/j.jpowsour.2012.01.076

[59] Dong Y, Hampshire S, Zhou J, Dong X, Lin B, Meng G (2011) Combustion synthesis and characterization of Cu–Sm co-doped CeO_2 electrolytes. J Eur Ceram Soc 31:2365–2376. doi:10.1016/j.jeurceramsoc.2011.04.037

[60] Jinping L (2015) Low temperature fabrication of dense gadolinia-doped ceria electrolyte with enhanced electrical conductivity. Electrochim Acta 178:321–328. doi:10.1016/j.electacta.2015.07.182

[61] Kilner JA, Brook RJ (1982) A study of oxygen ion conductivity in doped non-stoichiometric oxides. Solid State Ionics 6:237–252. doi:10.1016/0167-2738(82)90045-5

[62] Schwarz K (2006) Materials design of solid electrolytes. PNAS 103(10):3497. doi:10.1073/pnas.0600327103

[63] Seo DJ, Ryu KO, Park SB, Kim KY, Song RH (2006) Synthesis and properties of $Ce_{1-x}Gd_xO_{2-x/2}$ solid solution prepared by flame spray pyrolysis. Mater Res Bull 41:359–366. doi:10.1016/j.materresbull.2005.08.012

[64] Torrens R, Sammes NM, Tompsett G (2004) Characterization of Pr- and Sm-doped $Ce_{0.8}Gd_{0.2}O_{2-\delta}$. J Electroceram 13(1):683–689. doi:10.1007/s10832-004-5176-x

[65] Verkerk MJ, Keizer K, Burggraaf AJ (1980) High oxygen ion conduction in sintered oxides of the Bi_2O_3–Er_2O_3 system. J Appl Electrochem 10:81–90. doi:10.1007/BF00937342

[66] Huang W, Shuk P, Greenblatt M (1997) Properties of sol–gel prepared $Ce_{1-x}Sm_x0_{2-x/2}$ solid electrolytes. Solid State Ionics 100:23–27. doi:10.1016/S0167-2738(97)00309-3

[67] Sanghavi R, Devanathan R, Nandasiri MI, Kuchibhatla S, Kovarik L, Thevuthasan S, Prasad S (2011) Integrated experimental and modeling study of the ionic conductivity of samaria-doped ceria thin films. Solid State Ionics 204:13–19. doi:10.1016/j.ssi.2011.10.007

[68] Thangadurai V, Weppner W (2004) $Ce_{0.8}Sm_{0.2}O_{1.9}$: characterization of electronic charge carriers and application in limiting current oxygen sensors. Electrochim Acta 49:1577–1585. doi:10.1016/j.electacta.2003.11.019

[69] Lübke S, Wiemhöfer HD (1999) Electronic conductivity of Gd-doped ceria with additional Pr-doping. Solid State Ionics 117:229–243. doi:10.1016/S0167-2738(98)00408-1

[70] Bellino MG, Lamas DG, Walsöe de Reca NE (2006) Enhanced ionic conductivity in nanostructured heavily doped ceria ceramics. Adv Funct Mater 16:107–113. doi:10.1002/adfm.200500186